minerals

Article

Geology and Petrography of Uraniferous Bitumens in Permo-Carboniferous Sediments (Vrchlabí, Czech Republic)

Martina Havelcová [1], Ivana Sýkorová [1], Miloš René [1], Jiří Mizera [1,2,*], Miroslav Coubal [1], Vladimír Machovič [1,3], Vladimír Strunga [2,4] and Viktor Goliáš [4]

1   Institute of Rock Structure and Mechanics, Czech Academy of Sciences, V Holešovičkách 41,
     182 09 Praha 8, Czech Republic; havelcova@irsm.cas.cz (M.H.); sykorova@irsm.cas.cz (I.S.);
     rene@irsm.cas.cz (M.R.); coubal@irsm.cas.cz (M.C.); vladimir.machovic@vscht.cz (V.M.)
2   Nuclear Physics Institute, Czech Academy of Sciences, Hlavní 130, 250 68 Husinec-Řež, Czech Republic;
     strunga@ujf.cas.cz
3   Central Laboratories, University of Chemistry and Technology Prague, Technická 5,
     166 28 Praha 6, Czech Republic
4   Faculty of Science, Charles University, Albertov 6, 128 00 Praha 2, Czech Republic; wiki@natur.cuni.cz
*   Correspondence: mizera@ujf.cas.cz

Abstract: Uraniferous bitumens found in black shales from the Permian rocks at Vrchlabí in the Krkonoše Piedmont Basin (Czech Republic) were described and characterized petrologically and mineralogically. The Permian sediments originated from weathering products in metasediments and granitoids of the Krkonoše–Jizera and Orlice–Sněžník crystalline complexes. The organic matter contained up to 4.8 wt.% uranium, as uraninite grains. Elements associated with uraninite, such as Pb, Zr, Cu, and As, may have accumulated from epigenetic fluids in layers rich in organic matter during their late diagenesis. The bitumen structures were extremely heterogeneous, a feature attributed to the radiolytic effects of uranium. Amorphous bitumens, alternating with various forms of nodular and corroded bitumen types from multiple generations, were present. Low and highly altered bitumens with weak anisotropy were recognized, together with halo zones, with reflectance up to 4.37%. The halo zones differed in size, brightness, and reflectance, increasing from the edge to the center. Halos often revealed dark rims between uraninite inclusions and clear zones, originating probably as a result of weaker alterations in organic matter due to the presence of other inorganic components. Uranium concentration was the main factor controlling the degree of radiolytic alteration. The studied uraniferous bitumens are an excellent example of multistage formation and diverse evolution during burial and diagenesis.

Keywords: uraninite; bitumen; halos; bireflectance; radiolytic alteration

1. Introduction

The term uraniferous bitumens covers partially altered residues enriched in uranium minerals that derive from complex organic substances and are associated with petroleum, natural gas, or coal [1]. The uraniferous bitumens originate from migrating hydrocarbons and basal fluids but processes of evolution can also be in situ alteration of plant debris [2]. Hydrocarbons in sediments are transported by diffusion and uraniferous bitumens may be formed and immobilized as solids by radiolytic polymerization of formerly liquid hydrocarbons due to pre-existing detrital uraninite. Alternatively, migrating liquid hydrocarbons are mixed with hydrothermal/oxidizing solutions rich in uranyl ions, leading to precipitation of uraninite grains and formation of bitumen from liquid hydrocarbons. Either way, bitumens are polymerized and fill fractures and pores in rocks [3–8].

In 1928, Ellsworth [9,10] described uraniferous bitumen for the first time, using the term thucholite for the material. Since that time, other terms such as ucholite, carburane,

uraniferous pyrobitumen, or anthraxolite have been used to describe the association of uranium with organic matter in bituminous coal [11–13], lignites [14,15], or shales [16,17].

The contents and forms of uranium associated with sedimentary organic matter may vary from one deposit to another, and also locally. Uranium minerals can occur in inclusions of nanometer to micrometer scale, often homogeneously dispersed in the bitumen matrix. The long-term uranium–bitumen association can lead to damage of organic matter caused by radiolysis when α and β particles, and γ rays, are emitted from mineral grains containing uranium and thorium and their daughter products. The result is a structural breakdown of organic compounds that can be evidenced petrographically: vitrinite reflectance increases with uranium concentration [18], and bright aureoles—halos—are visible, surrounding uranium minerals and appearing under the microscope as circles or ellipses [19,20]. Radii of the halos in organic matter usually range from 40 to 60 µm, which is probably proportional to the shape of the mineral inclusions, energy of the emitted particles or rays, and density of the materials. The halos often have blurred features [8].

Uraniferous bitumens occur in several localities of the Czech Republic (Příbram, Butovice, Buchlov, Motol, Vrchlabí). For example, the vein fillings of uranium ore in Barrandian are essentially a heterogeneous mixture of fine-grained uraninite (partly coffinite and other ore minerals) relatively evenly dispersed in organic matter of an asphaltoid character [21]. Chemical reactions induced by the radiation of uranium and other radionuclides act destructively on the organic matter of bitumen and change the physical and chemical properties, as well as texture of the material [2,22,23]. The destructive effects of radiation are much more severe than the effects of oxidation, especially under sufficient uranium concentrations (~4–60 wt.%) and long periods (~270 million years) [21].

Uraniferous bitumen veins in black shales (Rudník Horizon) at Vrchlabí have already been studied and reported (e.g., [22,24]), but the data presented were scant, concentrations of uranium or other elements were either not given or limited, and detailed petrological and mineralogical analyses were not available. Studying the structure and properties of uraniferous organic matter in sedimentary rocks is an important topic, mainly in geological, nuclear, and environmental research focused on radioactive materials and wastes. The aim of this work is to characterize, petrologically and mineralogically, uraniferous bitumens (anthraxolites) in black shales from the Permian rocks at Vrchlabí in the Krkonoše Piedmont Basin (Czech Republic).

2. Geological Setting

The uraniferous bitumen deposit is hosted in the Vrchlabí Formation of the Krkonoše Piedmont Basin (KPB); see Figure 1. The Lower Permian Rudník Horizon represents the most extensive lacustrine deposits in the KPB. This basin belongs to a system of post-orogenic extensional/transtensional basins formed in the Bohemian Massif during Westphalian and Saxonian times (about Moscovian to Sakmarian, c. 310–280 Ma) [25,26]. The KPB is a ~1100 km^2 W-E elongated basin located on the Krkonoše–Jizera and Orlice–Sněžník crystalline complexes. The basin was filled with non-marine red beds of a total thickness of about 1800 m during the Upper Carboniferous and Lower Permian (Westphalian D—Sakmarian). There are several relatively thin grey and black shale, coaly, or variegated mudstone and carbonate interbeds penetrating the red bed infill, which are usually tens of meters thick [27].
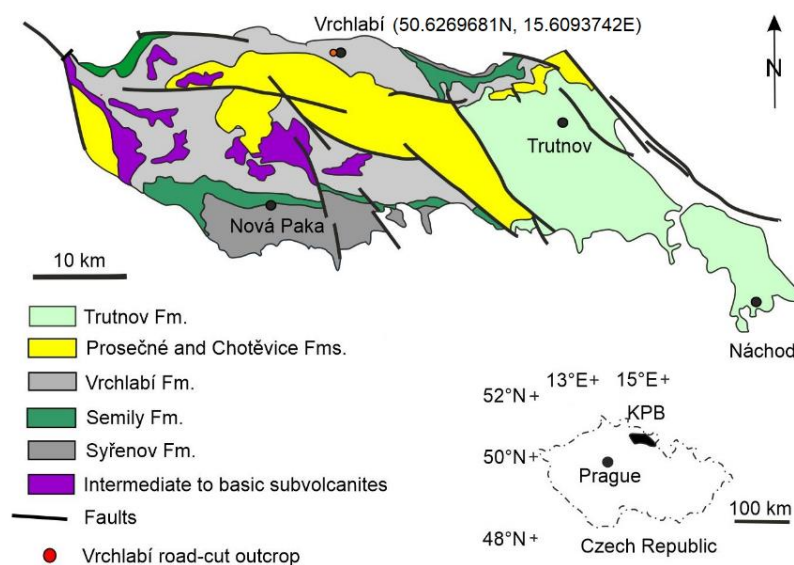
Figure 1. Simplified geological map of the Krkonoše Piedmont Basin (based on [28]).

Sediment accumulations were influenced by several different tectonic events. Their greatly different characters were mirrored in their different lithologies, and the culmination of tectonic events led to a stratigraphical hiatus [25,27]. The evolution of KPB was mostly influenced by the Sale tectonic event at the end of the Autunian. After the significant stratigraphical hiatus in the eastern part of the sedimentary space, formation of a new basin, elongated in the NW–SE direction started, adopting a function of the main sedimentation structure. The youngest stratigraphic units that remain in this basin were deposited in the Saxonian (Trutnov Formation) and connected to a younger formation of the lower Triassic age in the neighboring Intra-Sudetic Basin [25]. The shape of KPB in the northern part is limited by a tectonic structure, named by Chaloupský [29] as the South Krkonoše Tectonic Zone (Figure 1).

A well accessible outcrop of the original KPB sequence occurs as a road cut in the central part of the northern KPB margin at Vrchlabí. The lithological sequence opens in an SSW–NNE-trending, 1100 m long series of artificial exposures. It has been described in detail in [30,31] (Figure 2). These sediments are a part of the Vrchlabí Formation (Permian, Lower Autunian), representing a 300–500 m thick complex of mostly fluvial red beds and intercalated lacustrine strata. The road cut opens only the lower part of the Vrchlabí Formation, with an effective thickness of about 200 m. Fluvial sediments include flood-plain sandstones, which alternate with sheet-like fine-grained sandstones. Dominating sediments are medium- to coarse-grained sandstones, and lacustrine sediments are divided into three horizons.

The open part of the Vrchlabí Formation in this outcrop is mostly represented by the Rudník Horizon. The total thickness of the Rudník Horizon varies usually between 30 and 150 m. However, in this road cut, the horizon has evolved with an anomalous thickness of about 200 m. It consists of grey to green-grey siltstones, laminated claystones, limestones, and bituminous claystones. Intercalations of volcaniclastic beds are also observed [30]. The absence of coarser clastic deposits, even in nearshore facies, implies a relatively low sediment input, suggesting that the Vrchlabí road cut outcrop was located near the depocenter [26]. The lower part of the Vrchlabí Formation comprises predominantly siltstones that occur in a 500–620 m long part of the road cut. The upper part of the older Semily Formation (Upper Carboniferous) is represented predominantly by medium- to coarse-grained nonseparated sandstones and conglomerates with low-processed pebbles. At the Vrchlabí road cut, the internal structure of the South Krkonoše Tectonic Zone was also accessible to study. A flexural component is represented by the open tilting of layers, with

the dip growing to the south from approximately 16° in the southern part of the road cut to approximately 60° at the base of the Vrchlabí Formation.
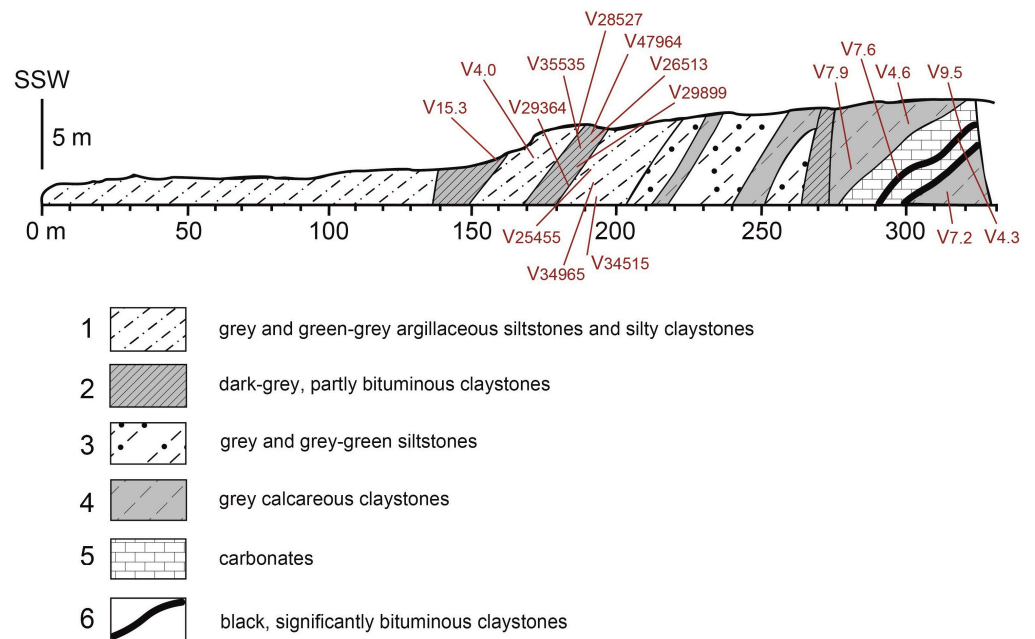

Figure 2. The lower part of the Vrchlabí formation (Permian, Lower Autunian), the upper part of the Rudník Horizon (based on [31], modified). Locations of samples studied are marked. Numbers in sample names indicate their U concentration (in ppm).

The sediments of both Permian-Carboniferous formations were subjected to quite an intense polyphase deformation. Hard argillaceous siltstones of the uppermost part of the Rudník Horizon at the beginning of the road cut form compact, finely stratified layers, dipping approximately 20° to the SSW. In the direction of the base, the lithology of sediments change, and in the road cut it is represented by interlaminating hard layers of carbonates and soft layers of laminated claystones and bituminous rocks. This, mechanically highly heterogeneous group of beds, suffered different types of deformation. The more compacted layers were flexed and fractured, whereas the soft layers were folded, mainly in the form of bituminous layers (Figure 3A,B). With this deformation event, the occurrence of uraniferous bitumens is related mostly with roofs of bituminous rock layers. In opened tectonic zones, different size pockets also occur. The latest deformation event, exposed in the road cut, is represented by faults of different sizes, and mainly in the E–W direction.
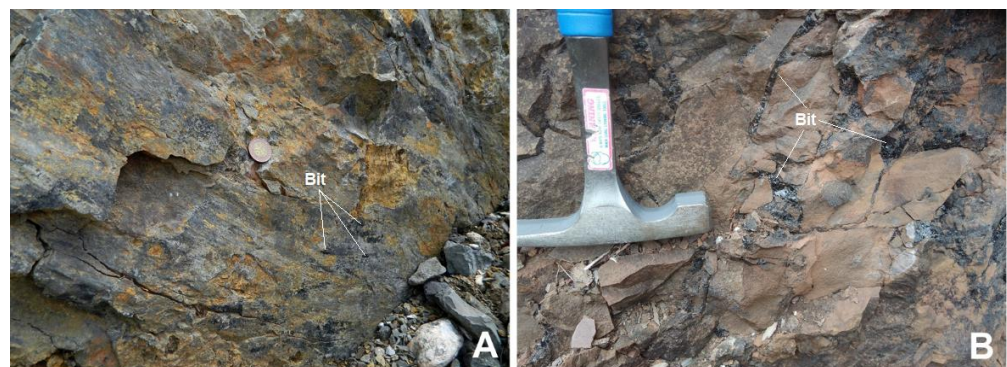

Figure 3. Occurrence of uraniferous bitumen in Permian black shales from the Vrchlabí Formation. (**A**) A deformed plane of dislocation in the Rudník Horizon with a small occurrence of a black, highly fractured uraniferous bitumen vein. (**B**) Veins and lenses of uraniferous bitumen in fractured shales.

Deformations of the older phase evidently post-dated the age of sedimentation of the Vrchlabí Formation, dated as Autunian (297–299 Ma) [25,27]. This deformation is probably coupled with the Sale tectonic event, dated at 292–294 Ma [27]. Late-stage deformations probably represent a distinctly younger tectonic reactivation of the South Krkonoše Tectonic Zone, coupled with elevation of the Krkonoše unit [32]. These deformation phases, discovered in different parts of this region, have been dated from Late Cretaceous to Paleocene (85–40 Ma) [33].

3. Materials and Methods

3.1. Samples and Their Basic Characterization

Seventeen samples from the Rudník Horizon of the Vrchlabí formation (50.6229831° N, 15.5963372° E; Figures 1 and 2) were collected. They were black shale samples with bitumen and uraniferous bitumens with different uranium contents and degree of alteration (Figures 3 and 4). Basic analyses were carried out: moisture content, ash, and total carbon. The elemental organic composition was determined using a CHNS/O microanalyzer Flash FA 1112 (Thermo Finnigan, Waltham, MA, USA). Organic carbon was determined by analysis after elimination of inorganic carbonates. Standard procedures of the International Organization for Standardization were used for the methods applied.
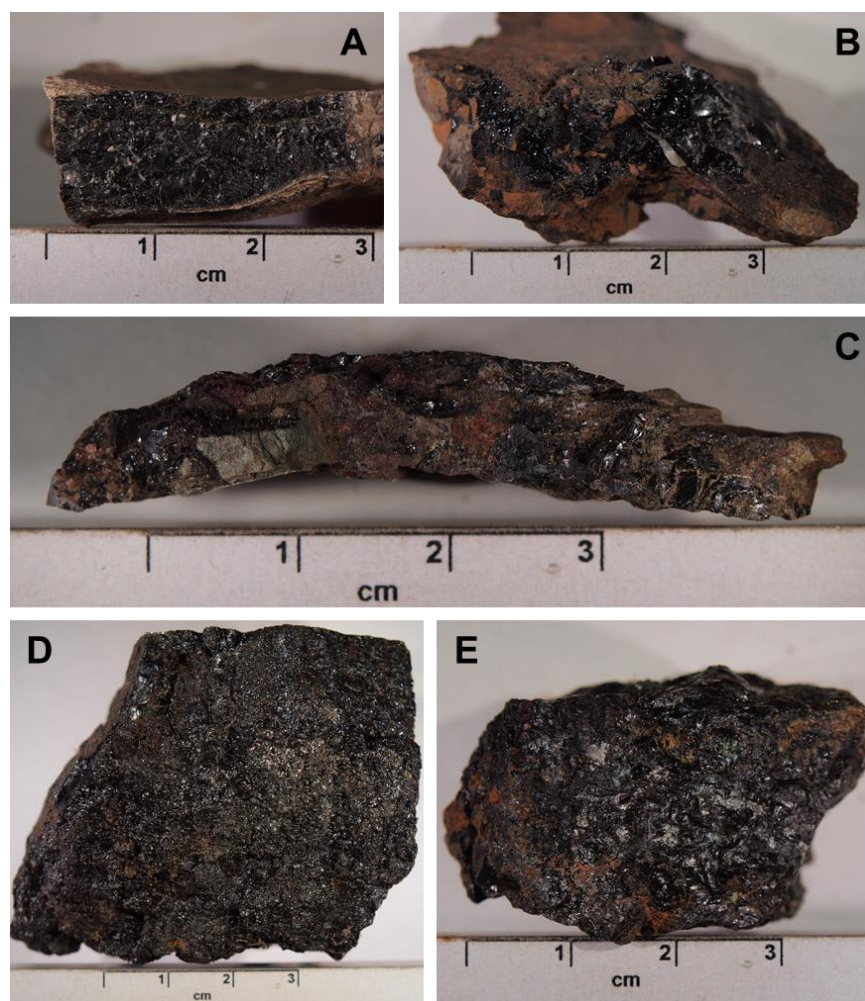

Figure 4. Macroscopic photographs of selected studied samples of black shales and uraniferous bitumen. Numbers in sample names indicate their U concentration (in ppm): (**A**) $V_{4.3}$; (**B**) $V_{7.6}$; (**C**) $V_{15.3}$; (**D**) V_{29364}; (**E**) V_{47964}.

3.2. Uranium Determination by INAA

Bulk uranium contents were determined by instrumental neutron activation analysis (INAA). INAA employed irradiation with neutrons in the LVR-15 research nuclear reactor of the Research Centre Řež. Uranium was determined in the long-time (2 h) irradiation mode by counting the 106.1 keV gamma line of ^{239}Np (daughter of ^{239}U). For quality control, reference materials NIST SRM 1633b (fly ash) and CRPG GS-N (granite) were analyzed together with samples using the same procedures. The usual potential of INAA for multielement analysis was greatly limited in samples with high contents of uranium, whose fission produced radionuclides that interfered with the determination of most elements. Details on the INAA experimental procedures have been published elsewhere [34].

3.3. Backscattered Scanning Electron Microscopy

Backscattered electron images were acquired to study the internal fabric of mineral aggregates and individual mineral grains using polished specimens. Chemical analyses were performed using an SX100 electron microprobe (Cameca, Gennevilliers, France) operating in wavelength dispersive mode (15 kV, 10 nA, and 2 μm beam width). The following standards and X-ray lines were used to minimize line overlaps: As-lammerite (As Lα), Ca-wollastonite (Ca Kα), Ce-CePO$_4$ (Ce Lα), Cu-lammerite (Cu Kα), Dy-DyPO$_4$ (Dy Lα), Er-ErPO$_4$ (Er Lα), Fe-almandine (Fe Kα), Gd-GdPO$_4$ (Gd Lβ), La-LaPO$_4$ (La Lα), Nd-NdPO$_4$ (Nd Lβ), P-fluorapatite (P Kα), Pb-vanadinite (Pb Mα), Pr-PrPO$_4$ (Pr Lβ), S-SrSO$_4$ (S Kα), Sc-ScVO4 (Sc Kα), Si-wollastonite (Si Kα), Sm-SmPO$_4$ (Sm Lβ), Sr-celestite (Sr Lα), Th-CaTh(PO$_4$)$_2$ (Th Mα), U-UO$_2$ (U Mβ), V-vanadinite (V Kα), Y-YAG (Y Lα), Zr-zircon (Zr Lα). Peak counting times were 20 s for all elements and one-half of the peak time for each background. Raw intensities were converted to element concentrations using an automated PAP matrix-correction software [35].

3.4. Optical Petrography

Maceral analysis and the measurement of random reflectance of vitrinite as a rank parameter [36] were carried out on samples. Polished sections were used in reflected, polarized, and ultraviolet light, using a BX51 microscope (Olympus America, Inc., New York, NY, USA) with Zeiss Photomultiplier MK3 system and fluorescence mode using an immersion lens with 40× and 100× magnification. The Pelcon point counter was used for maceral analysis producing 300 points per sample [5,22,37]. Random reflectance of unaltered vitrinite and bitumen particles, maximum and minimum reflectance values of amorphous bitumen (AB$_{am}$), partly mineralized bitumen (AB > Min), and halo (AB$_{Halo}$) of weakly and strongly altered bitumens were determined from particulate polished sections by SpectraVision software as described in detail in [12].

4. Results

4.1. Uranium, Ash, and Organic Carbon Contents

Uranium concentrations in the studied samples ranged from 4 ppm (4 mg/kg) to 47965 ppm (4.8 wt.%) and have been used (in ppm) as sample identifiers in their names. Ash yields (A^d) ranged between 12 wt.% and 93 wt.% corresponding to the type of sample, including black shales with variable bitumen content (V$_{4.0}$, V$_{4.3}$, V$_{4.6}$, V$_{7.2}$, V$_{7.6}$, V$_{7.9}$, V$_{9.5}$, V$_{15.3}$), and uraniferous bitumens (V$_{25455}$, V$_{26513}$, V$_{28527}$, V$_{29364}$, V$_{29899}$, V$_{34515}$, V$_{34965}$, V$_{35535}$, V$_{47964}$). Additionally, the total organic carbon content (TOC) reflected the type of sample: for the uraniferous bitumens this varied between 54.2 wt.% and 68.3 wt.%, and for the shale samples between 0.3 wt.% and 15.9 wt.%.

4.2. Organic Petrography

Sample V$_{4.0}$ represents a laminated black shale with dispersed organic matter including inertinite, liptinite, vitrinite, and bitumen (Figure 5). Other black shale samples had similar petrographic compositions with few exceptions. Samples V$_{7.2}$ and V$_{15.3}$ have lower contents of small organic particles with dispersed fine crystals of pyrite. Samples

$V_{4.3}$, $V_{7.6}$, and $V_{9.5}$ are rich in bituminite. Vitrinite reflectance (R_{rV}) of black shales varied between 0.77% and 0.96%, and bitumen reflectance (R_B) between 0.44% and 0.73% (Table 1). Bitumens had yellow to orange fluorescence colors.

Bitumen in uranium-enriched samples, found in vein fillings, had mean reflectance values (R_B) ranging from 0.54% to 0.69% (Table 1). However, more than 70 vol.% of the bitumens was radiolytically altered (Figure 5). The range of composition and optical properties of the uraniferous bitumens varied widely due to mineral inclusions and the degree of alteration. Pure bitumen to partly mineralized bitumen (e.g., bitumen between sparsely dispersed minerals, AB > Min, and compact formations of fine-grained minerals in bitumen, AB < Min), and full mineralized matter (Mineral matter) were distinguished. The degree of alteration changed from unaltered to weakly altered and strongly altered bitumens, revealing numerous textures ranging from amorphous matter (AB_{Am}) to light halos (AB_{Halo}) and very complex formations in terms of morphology and reflectance (Table 1 and Figure 5).

Figure 6 illustrates petrographical components of studied black shales and uraniferous bitumens. Unaltered, mineral-free solid amorphous bitumen with a yellow to orange fluorescence color, and darker, weakly altered bitumen (WAB) up to lighter, strongly altered bitumen (SAB) with shades of grey to white color were discovered. With increasing uranium content, the proportion of SAB, and mainly the abundance of halo zones (AB_{halo}), increased systematically (Figure 7). Amorphous altered bitumen (AB_{am}), sparsely mineralized bitumen (AB > Min), and dark halo zones showed weaker changes, visible in reflectance and bireflectance values (R_{minWAB}, R_{maxWAB}, and B_{WAB}) in relation to uranium concentrations (Table 1). SAB, also including halo (AB_{Halo}), amorphous (AB_{am}), and sparsely mineralized bitumen (AB > Min), revealed increasing maximum reflectance values (R_{maxSAB}, $R_{maxHalo}$) from 2.97% to 4.37% (Table 1). Additionally, the minimum reflectance values (R_{minSAB}) raised from 2.51% to 3.31% with increasing uranium content, as well as bireflectance (B_{SAB}, B_{Halo}), i.e., the difference between maximum and minimum reflectance values [23,36]. The values $B_{WAB} < 0.44\%$ for WAB, $B_{SAB} < 0.68\%$ for amorphous SAB, and up to 1.04% for light zones of halo (B_{Halo}) were found.
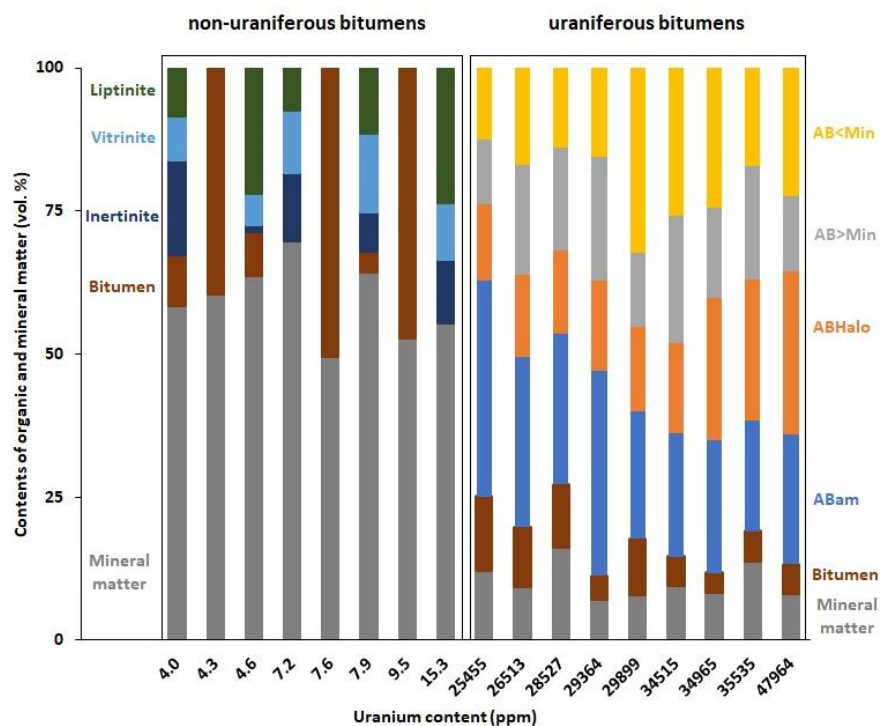
Figure 5. Organic and mineral matter contents in bitumens showing relationships between uranium content and petrographic components including forms of bitumen. Altered organic matter: AB_{am}—amorphous altered bitumen; AB_{Halo}—content of circular and irregular light and dark zones around uraninite grains; AB > Min—altered bitumen between sparsely dispersed minerals; AB < Min—compact formations of fine-grained minerals in altered bitumen.

Table 1. Reflectance values (%) of primary and altered organic matter in primary shales and uraniferous bitumens: R_{rV}—random reflectance of vitrinite; R_B—reflectance of unaltered bitumen; σ—standard deviation; n—number of measured points; R_{minWAB}—minimum reflectance of weakly altered bitumen (WAB); R_{maxWAB}—maximum reflectance of WAB; B_{WAB}—bireflectance of WAB; R_{minSAB}—minimum reflectance of strongly altered bitumen (SAB); R_{maxSAB}—maximum reflectance of SAB; B_{SAB}—bireflectance of SAB; $R_{maxHalo}$—maximum reflectance of light zones of halo and irregular zones around uraninite grains; B_{Halo}—bireflectance of light zones of halo and irregular zones around uraninite grains; n.i.—not identified. Numbers in sample names indicate their U concentration (in ppm).

| Sample	Reflectance of Unaltered Organic Matter						Reflectance and Bireflectance of Radiolytically Altered Bitumen in Polarized Light							
	R_{rV}	σ	n	R_B	σ	n	R_{minWAB}	R_{maxWAB}	B_{WAB}	R_{minSAB}	R_{maxSAB}	B_{SAB}	$R_{maxHalo}$	B_{Halo}
$V_{4.0}$	0.87	0.08	20	0.44	0.07	18	n.i.	n.i.	n.i.	n.i.	n.i.	n.i.	n.i.	n.i.
$V_{4.3}$	n.i.	-	-	0.66	0.11	20	n.i.	n.i.	n.i.	n.i.	n.i.	n.i.	n.i.	n.i.
$V_{4.6}$	0.82	0.08	20	0.54	0.08	15	n.i.	n.i.	n.i.	n.i.	n.i.	n.i.	n.i.	n.i.
$V_{7.2}$	0.96	0.09	15	0.73	0.12	15	n.i.	n.i.	n.i.	n.i.	n.i.	n.i.	n.i.	n.i.
$V_{7.6}$	n.i.	-	-	0.51	0.09	50	n.i.	n.i.	n.i.	n.i.	n.i.	n.i.	n.i.	n.i.
$V_{7.9}$	0.89	0.08	20	0.65	0.10	20	n.i.	n.i.	n.i.	n.i.	n.i.	n.i.	n.i.	n.i.
$V_{9.5}$	n.i.	-	-	0.53	0.09	20	n.i.	n.i.	n.i.	n.i.	n.i.	n.i.	n.i.	n.i.
$V_{15.3}$	0.77	0.07	18	n.i.	-	-	n.i.	n.i.	n.i.	n.i.	n.i.	n.i.	n.i.	n.i.
V_{25455}	n.i.	-	-	0.54	0.07	15	0.80	1.05	0.25	2.51	2.97	0.46	3.35	0.84
V_{26513}	n.i.	-	-	0.66	0.08	17	1.03	1.26	0.23	2.72	3.28	0.56	3.45	0.73
V_{28527}	n.i.	-	-	0.67	0.08	15	1.05	1.39	0.34	2.77	3.33	0.56	3.53	0.76
V_{29364}	n.i.	-	-	0.65	0.06	18	1.00	1.37	0.37	2.79	3.37	0.58	3.69	0.90
V_{29899}	n.i.	-	-	0.65	0.08	18	1.01	1.34	0.33	3.13	3.76	0.63	3.86	0.73
V_{34515}	n.i.	-	-	0.66	0.09	17	1.05	1.42	0.37	3.25	3.89	0.64	4.04	0.79
V_{34965}	n.i.	-	-	0.67	0.08	45	1.04	1.48	0.44	3.31	3.96	0.65	4.35	1.04
V_{35535}	n.i.	-	-	0.67	0.05	16	1.09	1.47	0.38	3.29	3.95	0.66	4.28	0.99
V_{47964}	n.i.	-	-	0.69	0.08	45	1.09	1.49	0.40	3.31	3.99	0.68	4.37	1.00
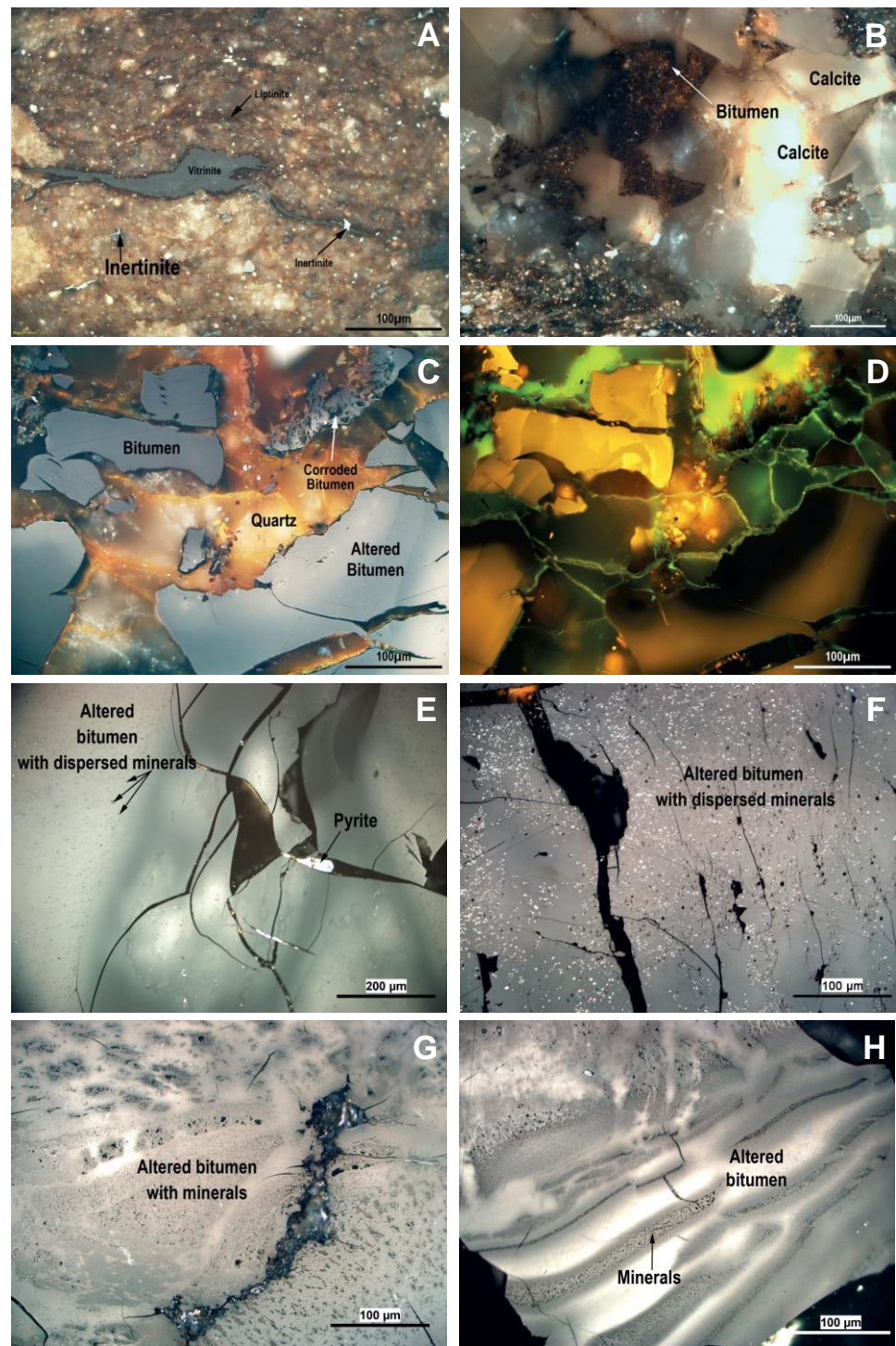
Figure 6. *Cont.*
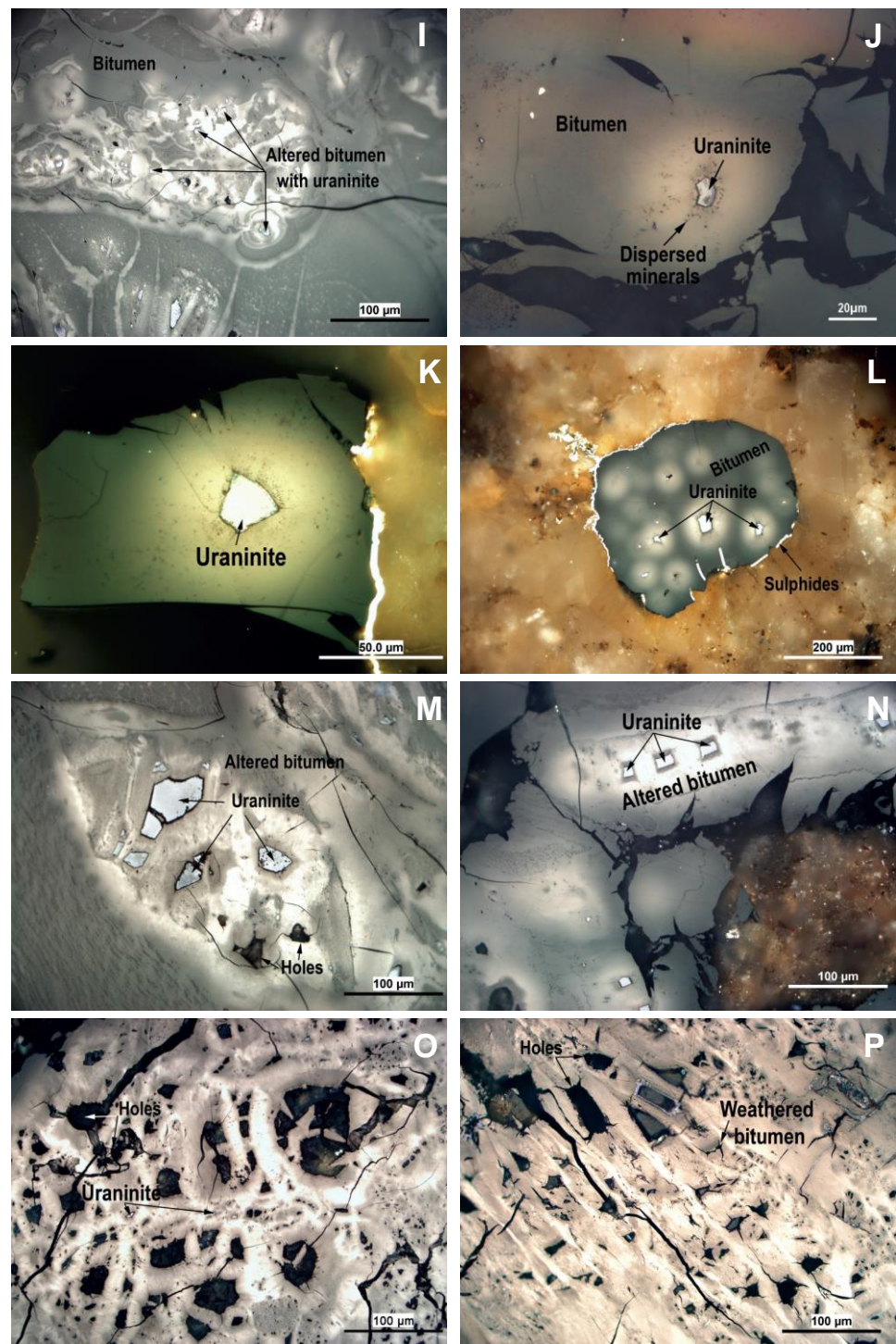
Figure 6. Petrographical components of black shales and uraniferous bitumens. Numbers in sample names indicate their U concentration in ppm ($V_{ppm\,U}$). Reflected light microscopy, if not stated otherwise. (**A**) Vitrinite particles in clayey matrix with dispersed liptinite and inertinite macerals ($V_{7.9}$). (**B**) Unaltered bitumen between calcite grains in veins of black shale ($V_{4.0}$). (**C,D**) Unaltered dark amorphous bitumen and radiolytically altered and corroded amorphous bitumen in a quartz vein (V_{28527}); C—reflected light microscopy, D—fluorescence mode. (**E**) Transformations of amorphous weakly altered bitumen to strongly radiolytically altered bitumen with dispersed fine mineral particles (V_{25455}). (**F**) Partly radiolytically altered amorphous bitumen with dispersed grains of pyrite, quartz, uraninite, and Fe, Ti oxides (V_{29364}). (**G**) Altered bitumen with uraniferous and other minerals

of variable grain sizes and its agglomerates around the crack (V_{29899}). (**H**) Fine-grained uraninite fillings of longitudinal cracks and strips between non-mineralized high reflective and altered bitumen (V_{34515}). (**I**) Complicated nodular texture with markedly light zones around uraninite grains lined with a layer of amorphous bitumen over densely mineralized bitumen with quartz and uraninite microparticles with small bright halos (V_{34956}). (**J**) Altered amorphous bitumen with a less reflective halo around a uraninite inclusion lined by a zone of sparsely dispersed fine-grained minerals (V_{25455}). (**K**) Large grain of uraninite with a simple unlimited high reflective halo in weakly altered bitumen (V_{28527}). (**L**) Bitumen cluster with a group of halos around differently sized uraninite grains, lined with pyrite and enclosed in carbonate (V_{26513}). (**M**) Light and dark zones around distinctive grains of U minerals and holes after fallen mineral grains closed by a layer of altered bitumen transitioning into a gray fine-grained quartz layer (V_{34956}). (**N**) Variously altered bitumens with distinct grains of uranium mineral with regular halos formed by thin darker and wider light zones in a quartz-clay vein in V_{35535}. (**O**) An interesting texture formed by fields of darker and light bitumen around grains of uranium mineral and holes of various sizes (V_{47964}). (**P**) Weathered and variable altered bitumen with vertical and horizontal crack networks, with mineral grains and holes left by them (V_{47964}).
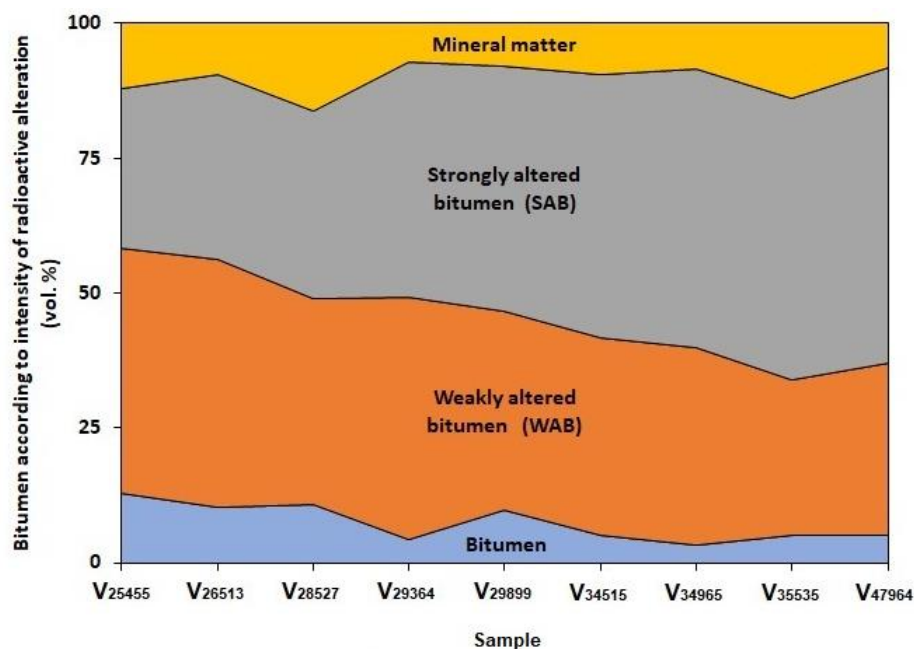

Figure 7. Altered organic matter and mineral matter showing relationships between uranium content and forms of bitumen. Numbers in sample names indicate their U concentration (in ppm).

Diversity in morphology, reflectance, fluorescence, and mineralogy was visible in the dark (WAB) and light (SAB) amorphous altered bitumens (Figure 6C–E), in finely mineralized (AB > Min) forms (Figure 6C,E,F), densely mineralized (AB < Min) forms (Figure 6G,H,I,M), in widespread halo (AB_{Halo}) formations (Figure 6J,K), and irregular light and inner darker zones (Figure 6N–P) around radioactive grains of uraninite. The abundance of alteration signs increased with higher uranium concentration. Contraction and oxidation cracks (Figure 6F,O,P) were observed in samples V_{25455}, V_{34515}, and V_{47964} as signals of an increased degree of weathering/oxidation.

Mineral matter (Figure 5) was represented as a mixture of individual grains of uraninite (Figure 6C,E,J–P), quartz (Figure 6C,D,J,K), pyrite, Fe and Ti oxides, and other accessory minerals of various size, and detritus from the surrounding rocks and vein fillings formed by quartz, clay minerals, and carbonates (Figure 6C,D,K,L,N).

4.3. Uranium Facies

Uraniferous bitumen occurs as crack fillings in irregular lenses and similar nodule-like structures, usually with irregular margins. The bitumen contains small anhedral inclusions of uraninite in sizes between 2 and 80 μm (Figure 8A), together with similar inclusions of nickel–cobalt sulpharsenides (gersdorfite), and rarely, chalcopyrite and pyrite. Irregular lenses, veins, and veinlets of quartz and Fe-hydroxides are also present. Rarely, uranium-rich secondary minerals (zeunerite) are visible (Figure 8B). In partly altered bitumens, the small inclusions of uraninite are surrounded with light zones which resemble radiolytic halos (Figure 8C). Their size, however, does not match the range of α particles in this kind of matrix (cf. Figure 6K–N) and should be interpreted differently, e.g., by uraninite dissolution and diffusion into the bitumen matrix.
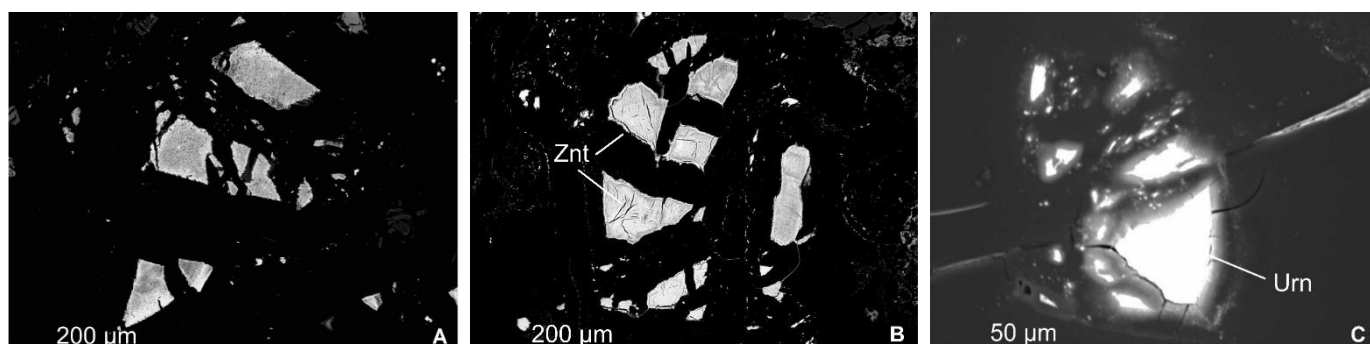

Figure 8. Back-scattered electron images of: (**A**) uraninite inclusions; (**B**) zeunerite (Znt) inclusions in partly altered bitumen; (**C**) lighter zones around small inclusions of uraninite (Urn).

The UO_2 content in uraninite analyzed was variable, ranging from 79.0 wt.% to 85.2 wt.%. All other constituents varied greatly, as documented in Table 2 presenting the composition of a representative sample, V_{28527}. The following variations were observed in the minor constituents: PbO 2.3–4.9 wt.%; CaO 1.9–3.0 wt.%; FeO 0.8–2.0 wt.%; SiO_2 0.6 wt.%–1.6 wt.%; ZrO_2 0.5–0.9 wt.%; Y_2O_3 0.2–0.3 wt.%; ThO_2 was below the detection limit of 0.07 wt.%. According to the correlation analysis carried out with compositions of uraninite located in spots (Table 3), strong positive correlations (expressed by the Pearson coefficient values) existed between ZrO_2 and FeO (+0.88), CuO (+0.84), and PbO (+0.73). Positive correlations were also found between As_2O_5 and CuO (+0.65), and UO_2 and CaO (+0.67). Strong negative correlations occurred between UO_2 and ZrO_2 (−0.91), CuO (−0.88), and FeO (−0.87).

Table 2. Representative compositions (wt.%) of uraninite grains in sample V_{28527} (b.d.l.—below detection limit: 0.01–0.04 wt.% for most elements, 0.1–0.3 wt.% for rare earth elements).

Oxide	V_{28527}, Analyse No.						
	1	2	3	4	5	6	7
UO_2	83.69	81.87	82.17	84.03	85.22	84.63	84.86
ThO_2	0.01	b.d.l.	b.d.l.	b.d.l.	b.d.l.	b.d.l.	b.d.l.
FeO	1.19	1.20	1.24	1.00	1.00	0.93	0.78
CaO	2.64	2.72	2.44	2.95	2.77	2.91	2.67
CuO	0.59	1.47	0.97	0.07	b.d.l.	b.d.l.	b.d.l.
SiO_2	0.94	1.03	1.02	0.81	0.91	0.92	1.17
ZrO_2	0.51	0.73	0.88	0.56	0.66	0.57	0.56

Table 2. *Cont.*

Oxide	V_{28527}, Analyse No.						
	1	2	3	4	5	6	7
PbO	3.98	4.11	4.15	3.43	3.26	3.09	2.85
P_2O_5	0.41	0.27	0.14	0.39	0.34	0.33	0.37
V_2O_5	0.37	0.19	0.35	0.25	0.20	0.18	0.14
As_2O_5	0.78	0.77	0.82	0.78	0.77	0.84	0.80
SO_3	0.01	0.09	b.d.l.	0.13	0.01	0.08	0.00
La_2O_3	b.d.l.	0.01	b.d.l.	b.d.l.	b.d.l.	b.d.l.	b.d.l.
Ce_2O_3	b.d.l.	0.16	b.d.l.	0.11	b.d.l.	b.d.l.	b.d.l.
Pr_2O_3	b.d.l.	0.17	0.26	0.06	b.d.l.	0.06	0.24
Nd_2O_3	0.19	0.19	0.31	0.19	0.26	0.24	0.22
Sm_2O_3	b.d.l.	b.d.l.	b.d.l.	b.d.l.	b.d.l.	b.d.l.	0.13
Gd_2O_3	b.d.l.	0.03	0.40	0.05	b.d.l.	0.26	b.d.l.
Dy_2O_3	0.13	b.d.l.	b.d.l.	b.d.l.	0.09	b.d.l.	b.d.l.
Er_2O_3	b.d.l.	0.13	0.05	b.d.l.	0.08	0.10	b.d.l.
Y_2O_3	0.19	0.29	0.22	0.26	0.23	0.21	0.30
Total	95.63	95.43	95.42	95.07	95.80	95.35	95.09

Table 3. Pearson coefficient values of uraninite compositions in analyzed spots.

Oxide	P_2O_5	SiO_2	SO_3	UO_2	CaO	CuO	FeO	V_2O_5	Y_2O_3	PbO	ZrO_2
As_2O_5	−0.42	−0.53	−0.12	−0.55	−0.63	0.65	0.48	−0.04	−0.20	0.23	0.33
ZrO_2	−0.46	0.16	−0.19	−0.91	−0.61	0.84	0.88	0.00	−0.36	0.73	
PbO	−0.42	0.01	−0.02	−0.70	−0.55	0.74	0.76	0.08	−0.43		
Y_2O_3	0.22	0.14	0.14	0.32	0.43	-0.39	−0.55	−0.02			
V_2O_5	0.27	−0.09	0.03	−0.09	0.06	0.03	0.14				
FeO	−0.39	−0.03	−0.20	−0.87	−0.71	0.90					
CuO	−0.53	−0.12	−0.24	−0.88	−0.77						
CaO	0.65	−0.10	0.03	0.67							
UO_2	0.48	−0.06	0.17								
SO_3	−0.01	0.06									
SiO_2	−0.18										

5. Discussion

Radiolytic alteration of organic matter is an interesting phenomenon causing changes in optical properties and morphology. The volume of unaltered bitumen, forms and abundance of altered bitumen (Figure 5), the presence of halos, values of their reflectance and bireflectance (Table 1), and fluorescence (Figure 6C,D) are effects and parameters that were affected and related to the occurrence of uranium in bitumens. The effects of radiation on organic structure and maturation of organic matter have been studied using various techniques in various materials such as organic-rich shales, carbon seam reefs, amber, carboniferous limestone, and carbonaceous debris in sandstones (e.g., [20,23,38–40]), and mainly in samples from deposits where uranium-bearing solutions and hydrocarbon fluids played a main role in the uranium enrichment (e.g., [3,41–44]). Various approaches and behaviors of organic matter were summarized by Landais [45].

5.1. Bitumen Morphology and Formation

In studied samples from Vrchlabí, reflected light microscopy as well as fluorescence microscopy showed layers of amorphous bitumen, alternating with various forms from multiple generations of nodular and corroded bitumen types. An illustrative example is a microbreccia in sample V_{28527} (Figure 6C,D). This may have been created from solid bitumen crushed by penetrating quartz and indicates the existence of several generations of hydrocarbons. There is a visible dark unaltered amorphous bitumen (left side of the image) without uraninite inclusions and with shades of yellow fluorescence. The bitumen particle

in the lower right part of the image documents a certain degree of bitumen alteration around uraninite microinclusions, and in the upper part of the image there is a bitumen relic that was corroded by inorganic fluids. Such diversity in the degree of alteration and in textures from simple to very complex formations originated from the interaction of fluid phases, formed by migrating hydrocarbons and hydrothermal uranium-bearing solutions.

The origin of the potential source of U and Cu in mineralization and hydrothermal uranium-bearing solutions is associated to infiltration of these sediments during their later diagenesis. The Permian basic tuffs were a source of Cu [46,47]. The detailed provenance analysis of the Permian sandstones and conglomerates [28] has shown that the sediments originated from weathering of metasediments and granitoids of the Krkonoše–Jizera and Orlice–Sněžník crystalline complexes. The origin of small uranium deposits occurring in the Jizera–Kowary crystalline unit, which is a part of the Krkonoše–Jizera crystalline complex (e.g., Kowary, Miedzianka), is related to intrusion of the Krkonoše granite pluton [48]. However, the major granite type of this pluton, the porphyritic biotite granite, is distinctly enriched in Th (24–36 ppm) and displays relatively low contents of U (4–5 ppm). Therefore, the source of U in uraninite in the uraniferous bitumens from Vrchlabí could be related to Cu-enriched epigenetic fluids generated during diagenesis of the Permian sediments, as indicated by co-occurrence of uraninite and U, Cu-bearing minerals such as zeunerite.

Bitumen was formed from hydrothermal solutions and vapors containing liquid and gaseous hydrocarbons that travelled through cracks and cavities of various sizes and shapes to the surface. The pressure within the rock was increasing, and gaseous and liquid hydrocarbons were expelled to migrate through primary porosity [49]. In larger cavities, the gases expanded and subsequently cooled and condensed due to the cooling effects of the rocks. This led to the production and accumulation of bitumen, occurring in rocks in the form of amorphous vein fillings and nodules with rounded to irregular contours. Fluorescence microscopy characterized bitumen nodules (Figure 6D), revealing that the nodules have a complex history with several phases of bitumen growth associated with multiple pulses of hydrocarbon circulation.

Generally, mixing of uraniferous basal fluids with migrating hydrocarbon fluids through cracks and cavities played a prominent role in the formation of uraniferous nodules. The organic and inorganic phases were partially separated during the solidification of this fluid system; after dewatering of the soluble inorganic phase, its components precipitated, the organic phase polymerized, and the amorphous matter was formed [50]. The reduction of soluble uranyl ions to insoluble uraninite took place in this process. During diagenesis, metals accumulated in layers rich in organic matter [4,45,47].

Several stages of this process, and mixing of solutions or emulsions is documented in the diversity of bitumen–mineral phase structures (Figure 6E–I,M). Almost one third of samples consisted of smooth amorphous bitumen resembling a solidified gel with variable reflectance (Figure 6C,E,F), irregularly transitioning to sparsely (Figure 6E,F) or to more densely (Figure 6G,K,M) mineralized positions. The formation of fine-grained mineral particles in an amorphous mass (Figure 6E–I) can be attributed to the precipitation of inorganic components, especially uraninite and pyrite, during gel solidification, or to migration of quartz, Fe and Ti oxides, and clay mineral microparticles (Figure 6G,M) from the surrounding veins or sediments. The surface arrangements and orientation of the inorganic nanoparticles in the mineralized bitumen was influenced by the outflow of water (Figure 6G,M). The darker, densely and finely mineralized areas (Figure 6H,I,M) resembled a solidified suspension of uranium and a mixture of other mineral nanocrystals joined by an amorphous organic phase, in which pores were present. Figure 6H shows an interesting collomorphic texture with alternating light and dark bands, formation of which can be explained by precipitation of uranium phases in the form of gel, and the subsequent recrystallization of these gels by water leakage, and thus volume reduction. In contrast, the nodular structure with alternating light and dark areas in Figure 6J documents the existence of two types of fluids which, when transformed into gels, were split into differently altered

organic and inorganic phases. The dark granular mass in Figure 6L that is fine-grained quartz has a similar source.

Uraninite in the uraniferous bitumens containing up to 4.8 wt.% U, is characterized by higher PbO content (up to 4.9 wt.%), ZrO_2 (up to 0.9 wt.%), and a slightly unusual enrichment in CuO (up to 1.8 wt.%) and As_2O_5 (up to 1.2 wt.%). The enrichment of Cu and As is heterogeneous and could be related to submicroscopic inclusions of gersdorfite and similar Cu and As minerals. Increased enrichment in Zr was also found in uraninite from vein deposits in Egypt (up to 2.5 wt.% ZrO_2, [51]), and in uraninite from the Jáchymov vein deposit in the Bohemian Massif (up to 1.8 wt.% ZrO_2), which was also enriched in As (up to 6.1 wt.% As_2O_5) [52]. The enrichment in As was also identified in uraninite from the Kowary uranium deposit (Poland), occurring in metasediments of the Krkonoše crystalline unit. However, this uraninite had very low concentrations of Zr (1 ppm at maximum) [53].

5.2. Optical Anisotropy of Radiolytically Altered Bitumen. Radiation-Induced Halos

Due to the heterogeneous character of radiolytically altered matter, studied bitumens were split into two textural classes, readily turning from one to the other. Firstly, into the dark WAB (R_{maxWAB} up to 1.49%) forming the basis of amorphous bitumen and whose proportion in samples decreased with increasing concentrations of uranium (Figure 7). Secondly, into the bright SAB and halo zones with reflectances up to 4.37% ($R_{maxHalo}$), and with diminishing fluorescence. Both WAB and SAB showed weak optical anisotropy under cross-polarized reflected-light microscopy, which indicates the beginning of structural reorganization of molecular components. Additionally, minor changes in reflectance R_{minWAB}, R_{maxWAB}, and B_{WAB} document weak anisotropy in the less altered bitumen (Figure 6). However, the increasing values of reflectance and bireflectance with increasing uranium content (Table 1) are obvious and the anisotropy, although weak, is highest in the case of strongly altered halo zones (up to 1.04% B_{Halo}) and irregular formations around uraninite grains, indicating a higher order of structural parameters.

The weak anisotropy of radiolytically altered and highly reflective bitumens is associated with dehydrogenation and oxidation processes and may be associated with a poorer pressure effect or even the absence of pressure in the system. Such a type of bitumen was also found in the Paja Formation of Colombia (Cretaceous age) [54], where the results revealed a low three-dimensional arrangement of basic structural units at high reflectance and bireflectance values in thermally altered bitumens. These results support the role of pressure in the formation of anisotropy in carbonaceous materials, which emphasizes the importance of oriented stress during tectonic action in thermal processes during coalification and maturation, as has been investigated by many authors and summarized in [36].

The presence of a bright optical halo around radioactive inclusions is an optical phenomenon known for years and explained as a result of α and β particles, emitted from the mineral grains. The halo zones differ in size (mostly over 30 μm in diameter) and brightness. Reflectance values vary within a halo, which may be related to the character of the radiation energy transfer, size and shape of inclusions, and density of the organic matter changing with the degree of structural re-organization by the radiolytic alteration ([8], and references therein). Simple rounded or oval halos without surface relief (Figure 6J–L), with reflectances increasing from the edge (0.80% R_{minWAB}) to the center of the halo (3.53% $R_{maxHalo}$), predominate in bitumens with uranium concentrations up to 2.85 wt.% U (sample V_{28527}). Groupings of irregular and asymmetrical embossed and highly reflective structures around variously sized and often decayed uraninite grains prevailed in bitumens with higher uranium concentrations and with denser uranium mass (Figure 6M–P). The observed large grains of uraninite are very often torn and separated from each other, and often look like strings of beads (Figure 6M–O). This is also typical for kidney-shaped uranium mineral formations, which are also segmented [7,55]. The reflectance values of these formations reached the highest measured values R_{maxSAB} 3.99% and $R_{maxHalo}$ 4.37% (Table 1). This texture likely reflects fracturing of a former larger grain that occurred as bitumen, dried and precipitated simultaneously with or soon after uraninite formation.

The majority of halos in the uraniferous bitumens studied had dark rims between uraninite inclusions and a clear zone, with a width up to 30 μm, but usually 2–10 μm. The detailed microscopic examination of the samples showed reflectances lower than 1.09%, without fluorescence. The dark zones often had granular character (Figure 6J,M,O) and mainly inorganic origin based on nanograins of quartz, oxides of Fe, and other identified minerals. Origin of the rims cannot be precisely determined but it should be the result of weaker alteration of organic matter with a low concentration of uranium in the dark zones due to the presence of other minerals and inorganic components.

Small dark uraninite grains up to about 5 μm were concentrated in formations of various shapes from elongated to oval or circular (Figure 6J–L). Most of these grains were dispersed in organic matter or diffused in bitumens (Figure 6M). The large mineral inclusions showed no relationship with the bitumen fabric and are possibly of post-date development. They are too abundant to be detrital grains and must represent precipitation inside the bitumen, as has been induced experimentally by Rouzard et al. [56]. The uraninite grains in uraniferous bitumens were precipitated shortly after interaction between uranium-bearing fluids and migrating hydrocarbons, i.e., uranium precipitation was coeval with bitumen solidification.

6. Conclusions

The bitumen forms in black shales from the Rudník Horizon of the Vrchlabí formation are an excellent example of diverse evolution. The bitumen has rounded and lobate shapes with variable irregular textures, alternating with nodular and corroded types, which indicate their multistage formation and coalescence during migration of originally liquid or semi-liquid hydrocarbon fluids. The diversity of the bitumen-mineral phase structures indicates that bitumen was formed during burial, while hydrothermal solutions and vapors passing through the primary porosity were altered due to irradiation by either uraninite or uranyl containing basal fluids that were mixed with liquid hydrocarbons during diagenesis.

Optical properties and morphologies of the samples from Vrchlabí demonstrate their radiolytic alteration. The presence of uranium affected the content of unaltered bitumen, number and area density of halos, values of reflectance, as well as fluorescence; the uranium concentration was the main factor controlling the values of mean (R_{AB}) and maximum reflectance (R_{maxAB}) in amorphous, partly mineralized bitumens and halos. The maturity of radiolytically altered bitumens studied increased up to levels found in high rank coal or anthracite.

Uranium is present in the bitumens at concentrations up to 4.8 wt.% U as uraninite, which is partly enriched along with other elements (Pb, Zr, Cu, and As). Mineral particles are often fine-grained in bitumen with organized surface arrangements and orientations, and filling pores. Their generation can be attributed to precipitation processes after water evaporation or to mechanical breaking of the cavity walls. Additionally, the mineral grains are often fragmented, which reflects breaking of former larger grains.

Radiation-induced halos are visible around uraninite inclusions, and their shapes have been determined by the character of the inclusion. Higher uranium contents imply irregular and asymmetrical, embossed, and more reflective halo structures. Reflectance changes through a halo, and dark rims separate mineral inclusions and clear halos, probably as a result of alteration between organic matter and minerals with low concentrations of uranium.

Author Contributions: Conceptualization, M.H., V.M. and J.M.; methodology, I.S., M.H., M.R., V.S., M.C. and V.G.; investigation, I.S., M.H., M.R., M.C. and V.S.; resources, V.M., J.M. and M.H.; writing—original draft preparation, M.H., I.S., M.R., J.M. and V.S.; writing—review and editing, M.H., J.M., V.G. and V.S.; supervision, M.H. and J.M.; project administration, M.H. and J.M.; funding acquisition, V.M., J.M. and M.H. All authors have read and agreed to the published version of the manuscript.

Data Availability Statement: The data presented in the tables and figures are openly available on request from the corresponding author.

Conflicts of Interest: The authors declare no conflict of interest.

References

1.　Boyle, R.W. *Geochemical Prospecting for Thorium and Uranium Deposits*; Elsevier Scientific Pub. Co.: Amsterdam, The Netherlands, 1982; 507p, ISBN 0-444-42070-3.

2.　Křibek, B.; Žák, K.; Spangenberg, J.E.; Jehlička, J.; Prokeš, S.; Komínek, J. Bitumens in the late Variscan hydrothermal vein-type uranium deposit of Příbram, Czech Republic: Sources, Radiation-Induced Alteration and Relation to Mineralization. *Econ. Geol.* **1999**, *94*, 1093–1114. [CrossRef]

3.　Fuchs, S.H.J.; Schumman, D.; Williams-Jones, A.E.; Murray, A.J.; Couillard, M.; Lagarec, K.; Phaneuf, M.W.; Vali, H. Gold and uranium concentration by interaction of immiscible fluids (hydrothermal and hydrocarbon) in the Carbon Leader Reef, Witwatersrand Supergroup. *S. Afr. Precambrian Res.* **2017**, *293*, 39–55. [CrossRef]

4.　Křibek, B. The Role of Organic Substances in the Processes of Hydrothermal Mineralization. *Geol. Carpath.* **1981**, *32*, 605–614. Available online: http://www.geologicacarpathica.com/browse-journal/authors/bohdan-kribek/ (accessed on 26 April 2022).

5.　Jacob, H. Classification, structure, genesis and practical importance of natural solid oil bitumen ("Migrabitumen"). *Int. J. Coal. Geol.* **1989**, *11*, 65–79. [CrossRef]

6.　Jacob, H. Nomenclature, Classification, Characterization, and Genesis of Natural Solid Bitumen (Migrabitumen). In *Bitumens in Ore Deposits*; Parnell, J., Kucha, H., Landais, P., Eds.; Springer: Berlin/Heidelberg, Germany, 1993; pp. 11–27. [CrossRef]

7.　England, G.L.; Rasmussen, B.; Krapež, B.; Groves, D.I. The origin of uraninite, bitumen nodules, and carbon seams in Witwatersrand gold-uranium-pyrite ore deposits based on a Permo-Triassic analogue. *Econ. Geol.* **2001**, *96*, 1907–1920. [CrossRef]

8.　Machovič, V.; Havelcová, M.; Sýkorová, I.; Borecká, L.; Lapčák, L.; Mizera, J.; Křibek, B.; Krist, P. Raman mapping of coal halos induced by uranium mineral radiation. *Spectrochim. Acta A* **2021**, *246*, 118996. [CrossRef]

9.　Ellsworth, H. Thucholite, a Remarkable Primary Carbon Mineral from the vicinity of Parry Sound, Ontario. *Am. Mineral.* **1928**, *13*, 419–441. Available online: http://www.minsocam.org/ammin/AM13/AM13_419.pdf (accessed on 26 April 2022).

10.　Ellsworth, H. Thucholite and Uraninite from Wallingford Mine, Near Buckingham, Quebec. *Am. Mineral.* **1928**, *13*, 442–448. Available online: http://www.minsocam.org/ammin/AM13/AM13_442.pdf (accessed on 26 April 2022).

11.　Eskenazy, G.M.; Velichkov, D. Radium in Bulgarian coals. *Int. J. Coal. Geol.* **2012**, *94*, 296–301. [CrossRef]

12.　Sýkorová, I.; Křibek, B.; Havelcová, M.; Machovič, V.; Špaldoňová, A.; Lapčák, L.; Knésl, I.; Blažek, J. Radiation- and self-ignition induced alterations of Permian uraniferous coal from the abandoned Novátor mine waste dump (Czech Republic). *Int. J. Coal. Geol.* **2016**, *168*, 162–178. [CrossRef]

13.　Křibek, B.; Sýkorová, I.; Veselovský, F.; Laufek, F.; Malec, J.; Knésl, I.; Majer, V. Trace element geochemistry of self-burning and weathering of a mineralized coal waste dump: The Novátor mine, Czech Republic. *Int. J. Coal. Geol.* **2017**, *173*, 158–175. [CrossRef]

14.　Havelcová, M.; Machovič, V.; Mizera, J.; Sýkorová, I.; Borecká, L.; Kopecký, L. A multi-instrumental geochemical study of anomalous uranium enrichment in coal. *J. Environ. Radioactiv.* **2014**, *137*, 52–63. [CrossRef] [PubMed]

15.　Rallakis, D.; Michels, R.; Brouand, M.; Parize, O.; Cathelineau, M. The role of organic matter on uranium precipitation in Zoovch Ovoo, Mongolia. *Minerals* **2019**, *9*, 310. [CrossRef]

16.　Lecomte, A.; Cathelineau, M.; Michels, R.; Peiffert, C.; Brouand, M. Uranium mineralization in the Alum Shale Formation (Sweden): Evolution of a U-rich marine black shale from sedimentation to metamorphism. *Ore Geol. Rev.* **2017**, *88*, 71–98. [CrossRef]

17.　Liu, B.; Mastalerz, M.; Schieber, J.; Teng, J. Association of uranium with macerals in marine black shales: Insights from the Upper Devonian New Albany Shale, Illinois Basin. *Int. J. Coal. Geol.* **2020**, *217*, 103351. [CrossRef]

18.　Breger, I.A. The Role of Organic Matter in the Accumulation of Uranium: The Organic Geochemistry of the Coal-Uranium Association. In *Formation of Uranium Ore Deposits*; International Atomic Energy Agency (IAEA): Vienna, Austria, 1974; pp. 99–124. Available online: https://inis.iaea.org/search/search.aspx?orig_q=RN:6198393 (accessed on 26 April 2022).

19.　Gentry, R.V. Radiohalos in coalified wood: New evidence relating to the time of uranium introduction and coalification. *Science* **1976**, *194*, 315–318. [CrossRef]

20.　Leventhal, J.S.; Daws, T.A.; Frye, J.S. Organic geochemical analysis of sedimentary organic matter associated with uranium. *Appl. Geochem.* **1986**, *1*, 241–247. [CrossRef]

21.　Dubanský, A.; Jahoda, K.; Habersbergerová, A. Anthraxolite in the Barrandian part of the Bohemian Massif. *J. Geol. Sci. Technol. Geochem.* **1987**, *22*, 9–50.

22.　Parnell, J. Chemical Age Dating of Hydrocarbon Migration Using Uraniferous Bitumens, Czech-Polish Border Region. In *Bitumens in Ore Deposits*; Parnell, J., Kucha, H., Landais, P., Eds.; Springer: Berlin/Heidelberg, Germany, 1993; pp. 510–517. Available online: https://link.springer.com/chapter/10.1007/978-3-642-85806-2_28 (accessed on 26 April 2022).

23. Smieja-Król, B.; Duber, S.; Rouzaud, J.N. Multiscale organisation of organic matter associated with gold and uranium minerals in the Witwatersrand basin, South Africa. *Int. J. Coal. Geol.* **2009**, *78*, 77–88. [CrossRef]

24. Klubov, B.A. Prirodnyje bitumy Krkonošskogo predgornogo bassejna (Bitumens of the Krkonoše Mts. piedmont basin). *Otečestvennaja Geol.* **1993**, *9*, 3–9.

25. Tásler, R.; Prouza, V. *Podkrkonošská Pánev—Zhodnocení Geologických a Uhelně Ložiskových Poměrů (Krkonoše Piedmont Basin—Evaluation of Geology and Coal-Geology Relations)*; Czech Geologic Survey: Prague, Czech Republic, 1985; 60p.

26. Martínek, K.; Blecha, M.; Daněk, V.; Francŭ, J.; Hladíková, J.; Johnová, R.; Uličný, D. Record of paleoenvironmental changes in a Lower Permian organic rich lacustrine succession, integrated sedimentological and geochemical study of the Rudník member, Krkonoše Piedmont Basin, Czech Republic. *Palaeogr. Palaeoclimatol. Palaeoecol.* **2006**, *230*, 85–128. [CrossRef]

27. Opluštil, S.; Schmitz, M.; Kachlík, V.; Štamberg, S. Re-assessment of lithostratigraphy, biostratigraphy, and volcanic activity of the Late Paleozoic Intra-Sudetic, Krkonoše Piedmont and Mnichovo Hradiště basins (Czech Republic) based on new U-Pb CA-ID-TIMS ages. *Bull. Geosci.* **2016**, *91*, 399–432. [CrossRef]

28. Martínek, K.; Štolfová, K. Provenance study of Permian non-marine sandstones and conglomerates of the Krkonoše Piedmont Basin (Czech Republic): Exotic marine limestone pebbles, heavy minerals and garnet. *Bull. Geosci.* **2009**, *84*, 555–568. [CrossRef]

29. Chaloupský, J. *Geologie Krkonoš a Jizerských hor (Geology of the Krkonoše and Jizerské Hory Mts.)*; Academia: Prague, Czech Republic, 1989; 289p.

30. Šimůnek, Z.; Zajíc, J.; Drábková, J. *Paleontologické Zpracování Sběrů z Lokality Vrchlabí—Zářez Silnice na jz. Okraji Města (Paleontological Study of the Vrchlabí Road-Cut on the SE Town Margin)*; Czech Geological Survey: Prague, Czechoslovakia, 1990; 107p.

31. Prouza, V. *Permokarbon Západní a Centrální Části Podkrkonošské Pánve (Permian-Carboniferous Formations of the Western and Central Parts of the Krkonoše Piedmont Basin)*; Czech Geological Survey: Prague, Czech Republic, 2005; 13p, Available online: https://www.google.com/url?esrc=s&q=&rct=j&sa=U&url=http://www.geology.cz/svet-geologie/vylety/pruvodce/Permokarbon_zapadni_a_centralni_casti_podkrkonosske_panv.pdf (accessed on 26 April 2022).

32. Prouza, V.; Coubal, M.; Adamovič, J. Southeastern Continuation of the Lusatian Fault in the Western Krkonoše Mts. Piedmont Region. *Geosci. Res. Rep.* **2013**, *46*, 59–63. Available online: http://www.geology.cz/zpravy/en/detail/Zpravy_2012-11 (accessed on 26 April 2022).

33. Coubal, M.; Málek, J.; Adamovič, J.; Štěpančíková, P. Late Cretaceous and Cenozoic dynamics of the Bohemian Massif inferred from the paleostress history of the Lusatian Fault Belt. *J. Geodyn.* **2015**, *87*, 26–49. [CrossRef]

34. Mizera, J.; Řanda, Z. Instrumental neutron and photon activation analyses of selected geochemical reference materials. *J. Radioanal. Nucl. Chem.* **2010**, *284*, 157–163. [CrossRef]

35. Pouchou, J.L.; Pichoir, F. "PAP" $\varphi(\rho Z)$ Procedure for Improved Quantitative Microanalysis. In *Microbeam Analysis*; Armstrong, J.T., Ed.; San Francisco Press: San Francisco, CA, USA, 1985; pp. 104–106.

36. Taylor, G.H.; Teichmüller, M.; Davis, A.; Diessel, C.F.K.; Littke, R.; Robert, P. *Organic Petrology*; Gebrüder Borntraeger: Berlin/Stuttgart, Germany, 1998; 704p, ISBN 978-3-443-01036-2.

37. Jedwab, J. Significance and Use of Optimal Phenomenon in Uraniferous Caustobioliths. In *Coal Science. Advances in Chemistry No. 55*; Given, P.H., Ed.; American Chemical Society: Washington, DC, USA, 1966; pp. 119–132.

38. Havelcová, M.; Machovič, V.; Mizera, J.; Sýkorová, I.; René, M.; Borecká, L.; Lapčák, L.; Bičáková, O.; Janeček, O.; Dvořák, Z. Structural changes in amber due to uranium mineralization. *J. Environ. Radioactiv.* **2016**, *158–159*, 89–101. [CrossRef]

39. Khan, I.; Zhong, N.; Luo, Q.; Ai, J.; Yao, L.; Luo, P. Maceral composition and origin of organic matter input in Neoproterozoic-Lower Cambrian organic-rich shales of Salt Range Formation, upper Indus, Pakistan. *Int. J. Coal. Geol.* **2020**, *217*, 103319. [CrossRef]

40. Zhang, F.; Yangquan, J. Changes in physicochemical properties of organic matter by uranium irradiation: A case study from the Ordos Basin in China. *J. Environ. Radioactiv.* **2020**, *211*, 106105. [CrossRef]

41. Parnell, J. Mineralogy of Uraniferous Hydrocarbons in Carboniferous-Hosted Mineral Deposits, Great Britain. *Uranium* **1988**, *4*, 197–218. Available online: https://inis.iaea.org/search/search.aspx?orig_q=RN:20025730 (accessed on 26 April 2022).

42. Mossman, D.J.; Nagy, B. Solid bitumens: An assessment of their characteristics, genesis, and rolein geological processes. *Terra Nova* **1996**, *8*, 114–128. [CrossRef]

43. Mossman, D.J.; Gauthier-Lafaye, F.; Jackson, S.E. Black shales, organic matter, ore genesis, and hydrocarbon generation in the Paleoproterozoic Franceville Series, Gabon. *Precambrian Res.* **2005**, *137*, 253–272. [CrossRef]

44. Fuchs, S.; Williams-Jones, A.E.; Jackson, S.E.; Przybylowicz, W.J. Metal distribution in pyrobitumen of the Carbon leader reef, Witwatersrand Supergroup, South Afrika: Evidence for liquid hydrocarbon more fluids. *Chem. Geol.* **2016**, *426*, 45–59. [CrossRef]

45. Landais, P. Organic geochemistry of sedimentary uranium ore deposits. *Ore Geol. Rev.* **1996**, *11*, 33–51. [CrossRef]

46. Čadková, Z. Sedimentary Copper Deposits in the Carboniferous and Permian. In *Ore Deposits and Metallogeny of the Czechoslovak Part of the Bohemian Massif*; Bernard, J.H., Pouba, Z., Eds.; Academia: Prague, Czech Republic, 1986; pp. 259–260.

47. Kříbek, B. The role of organic matter in the metallogeny of the Bohemian Massif. *Econ. Geol.* **1989**, *84*, 1525–1540. [CrossRef]

48. Mochnacka, K.; Oberc-Dziedzic, T.; Mayer, W.; Pieczka, A. Ore mineralization related to geological evolution of the Karkonosze-Izera Massif (the Sudetes, Poland)—Towards a model. *Ore Geol. Rev.* **2015**, *64*, 215–238. [CrossRef]

49. Robb, L.J.; Meyer, F.M. The Witwatersrand Basin, South Africa: Geological framework and mineralization processes. *Ore Geol. Rev.* **1995**, *10*, 67–94. [CrossRef]

50. Parnell, J. Phanerozoic analogues for carbonaceous matter in Witwatersrand ore deposits. *Econ. Geol.* **1996**, *91*, 55–62. [CrossRef]

51. Shahin, H. Geochemical Characteristics and Chemical Electron Microprobe U-Pb-Th Dating of Pitchblende Mineralization from Gabal Gattar Younger Granite, North Eastern Desert, Egypt. *Open J. Geol.* **2014**, *4*, 24–32. [CrossRef]

52. René, M.; Dolníček, Z.; Sejkora, J.; Škácha, P.; Šrein, V. Uraninite, coffinite and ningyoite from vein-type uranium deposits of the Bohemian Massif (Central European Variscan Belt). *Minerals* **2019**, *9*, 123. [CrossRef]

53. Frimmel, H.E.; Schedel, S.; Brätz, H. Uraninite chemistry as forensic tool for provenance analysis. *App. Geoch.* **2014**, *48*, 104–121. [CrossRef]

54. Suárez-Ruiz, I.; Juliao, T.; Rodrigues, S.; Camean, I. Optical parameters and microstructural properties of Solid Bitumens of high reflectance (Impsonites). Reflections on their use as an indicator of organic maturity. *Int. J. Coal. Geol.* **2020**, *229*, 158–175. [CrossRef]

55. Eakin, P.A. Isotopic and petrographic studies of uraniferous hydrocarbons from around the Irish Sea Basin. *J. Geol. Soc. Lond.* **1989**, *146*, 663–673. [CrossRef]

56. Rouzard, J.N.; Oberlin, A.; Trichet, J. Interaction of Uranium and Organic Matter in Uraniferous Sediments. In *Advances in Organic Geochemistry*; Douglas, A.G., Maxwell, J.R., Eds.; Pergamon: Oxford, UK, 1980; pp. 505–516.